A Letters Journal Exploring the Frontiers of Physics

April 2014

EPL, **106** (2014) 14002 www.epljournal.org
doi: 10.1209/0295-5075/106/14002

# Continuum dynamics of elastocapillary coalescence and arrest

Z. Wei[1] and L. Mahadevan[1,2(a)]

[1] *School of Engineering and Applied Sciences, Harvard University - Cambridge, MA 02138, USA*
[2] *Department of Physics, Harvard University - Cambridge, MA 02138, USA*

received on 7 March 2014; accepted by D. Quéré on 30 March 2014
published online 11 April 2014

PACS 47.20.Dr – Surface-tension-driven instability
PACS 46.32.+x – Static buckling and instability
PACS 64.75.Yz – Self-assembly

**Abstract** – The surface-tension–driven coalescence of wet hair, nano-pillars and supported lamellae immersed in an evaporating liquid is eventually arrested elastically. To characterize this at a continuum level, we start from a discrete microscopic model of the process and derive a mesoscopic theory that couples the inhomogeneous dynamics of drying to the capillary forcing and elastic bending of the lamellae. Numerical simulations of the resulting partial differential equation capture the primary unstable mode seen in experiments, and the dynamic coalescence of the lamellae into dimers and quadrimers. Our theory also predicts the elastic arrest of the pattern or the separation of lamellar bundles into their constituents as a function of the amount of liquid left at the end of the process.

editor's choice Copyright © EPLA, 2014

Capillary coalescence arises in a number of systems, including particles at an interface as well as filaments and lamellae that are brought together by interfacial forces which drive aggregation. Sometimes, these systems coarsen indefinitely, while at other times elastic deformations eventually arrest the process. Examples of the former include particles at an interface driven together by capillary and/or magnetic forces where aggregation and assembly continue eventually leading to just a single cluster [1,2]. In contrast to the aggregation of free particles, elastic deformations of the bristles and lamellae eventually limit the coarsening leading to many finite-sized clusters [3–5]. Prior investigations of the elastocapillary coalescence of these systems have been primarily focused on understanding the final size of the bundle using energy minimization [4,6]. Exceptions include a phenomenological continuum mean-field theory [7] for arrested coarsening, and a discrete theory [8] for regular, ordered hierarchical aggregation. Here, we complement these studies using a long-wavelength continuum theory that imposes no hierarchical pattern *a priori* and is derived from a physically consistent microscopic picture that accounts for spatial/temporal variations driven by inhomogeneities in drying and eventually arrested by elasticity.

(a) E-mail: lm@seas.harvard.edu

We consider a one-dimensional array of evenly spaced mirco-lamellae that are made of the incompressible material with Young's modulus $E$, and have height $L$, thickness $h$ and uniform spacing $D$ [3] (see fig. 1). Each lamella is anchored at one end on a substrate and free at the other. The array is initially completely immersed in a liquid with an air-liquid surface tension $\sigma$. When the liquid evaporates, the liquid remains confined between two neighboring lamellae which define a cell. During this process, capillary forces associated with the liquid-air menisci between the free ends of the soft lamellae can cause them to deflect laterally and adhere together. In the experiment, we observe a cascade of successive sticking events that leads to a hierarchical bundling pattern: pairs of neighboring lamellae tilt towards each other to form a dimer; these dimers collapse to form quadrimers, and so on. This process repeats until the increasing elastic resistance eventually arrests the coarsening. After the liquid dries out, the bundles separate into lamellae if the adhesion between lamellae is not strong to counterbalance the elastic forces; otherwise they persist.

We adopt a Bloch-wave–like analysis [9] for our periodic mechanical system which consists of $2N$ vertical lamellae and the same volume of liquid $V$ confined in each cell. If $\overrightarrow{M}$ is the vector of moments on all plates and $\overrightarrow{\theta}$ is the

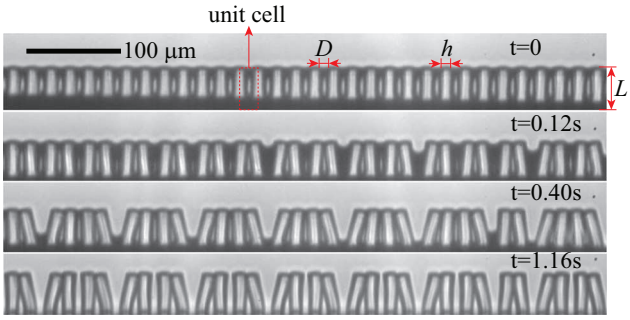


Fig. 1: (Colour on-line) (a) Experimental snapshots of 2-dimensional lamellar coalescence driven by an evaporating liquid. The lamellae are made of polydimethylsiloxane (PDMS) with pre-polymer and cross-linker weight ratio 10 : 1 and Young's modulus $E = 1.275\,\mathrm{MPa}$. The geometric parameters are pillar height $L$, thickness $h$, and spacing $D$ with $L = 4h = 4D = 40\,\mu\mathrm{m}$. The liquid is isopropyl alcohol (IPA), with an interfacial tension $\sigma = 0.022\,\mathrm{N/m}$. As the liquid evaporates, lamellae bundle to form dimers, quadrimers and other hierarchical structures. As the liquid dries out, bundles separate out in the reverse order if the surface adhesion due to contact is not strong enough to counterbalance the bending resistance.

vector of deflection angles of all plates, we can write

$$M_n = -k_c l^2 \partial_d^2 \theta_n + k_b \theta_n, \tag{1}$$

where $M_n$ is the local moment on the $n$-th plate, $\theta_n$ is the deflection angle of the $n$-th plate, $l = D + h$ is the size of the unit cell, $k_c(\sigma L, V/L^2)$ is the capillary stiffness, $k_b = Eh^3/3L$ is the bending stiffness (see appendix), and $\partial_d^2\theta_n = (\theta_{n+1} - 2\theta_n + \theta_{n-1})/l^2$ is the discrete Laplacian. Then the stiffness matrix $\mathrm{d}\vec{M}/\mathrm{d}\vec{\theta}$ has eigenvalues $s(f)$ and eigenvectors $\Psi(f)$ given by

$$s(f) = -2k_c\cos(f) + 2k_c + k_b, \tag{2}$$

$$\Psi(f) = \left[1, e^{if}, e^{2if}, \ldots, e^{i(2N-3)f}, e^{i(2N-2)f}, e^{-if}\right], \tag{3}$$

respectively, where $f = n\pi/N$ with $n = 1, 2, \ldots, 2N$.

From (2), we see that when $k_c \geq 0$, $s \geq k_b > 0$, and the vertical base state is stable. When $k_c < 0$, the smallest eigenvalue is $s(\pi) = 4k_c + k_b$ corresponding to $f = \pi$, reflecting the fact that stability is controlled by the competition between elasticity and capillarity. As $k_c = k_c(V)$, this eigenvalue can switch sign so that $s(\pi) < 0$ for a range of $V$ where the system is unstable. For this case, we see from (3) that the eigenvector of the primary mode is $[1, -1, 1, -1, \ldots, 1, -1]$, corresponding to the dimerization two-lamella-collapse mode observed from the experiments. Beyond the onset of instability, we have to numerically determine the aggregation dynamics using the discrete model [10]. Alternatively we can develop a long-wavelength continuum theory that unifies the linear and nonlinear dynamics of the system to explain elastically arrested phase separation.

In our continuum model, we consider a binary fluid that is composed of two constituents: the tips of the lamellae and gaps between them. Denoting $\phi$ as the concentration field of the binary fluid, with $\phi = -1$ corresponding to gaps and $\phi = 1$ to tips, the equation describing the phase separation is given by

$$\partial_t \phi = -\partial_x J = a_0 \partial_x^2 \frac{\delta U}{\delta \phi}, \tag{4}$$

where $\partial_t = \partial/\partial t$, $\partial_x = \partial/\partial x$, $\partial_x^2 = \partial^2/\partial x^2$ etc., and $J$ is the flux. The first equality in (4) follows from mass conservation and the last equality follows from the assumption that the flux is proportional to the gradient of the chemical potential $\partial_x(\delta U/\delta\phi)$, where $a_0$ is the diffusion constant and $U(\phi)$ is the free energy of the system that includes the bending energy of lamellae, the surface energy of the air-liquid interface, and the potential energy associated with the pressure gradient across the lamella. It is simpler to write the free energy $U(\theta)$, where $\theta$ is the deflection angle field, and then relate $\phi$ to $\theta$. In the linear deformation regime where $|\theta| \ll 1$,

$$U(\theta) = \int_0^{\mathcal{L}} \frac{M\theta}{2l}\mathrm{d}x, \tag{5}$$

where $\mathcal{L}$ is the system size, and $M$ is the local moment given by (1). In the continuum limit, letting $\theta(x) = \theta_n$, $\theta(x+l) = \theta_{n+1}$ and $\theta(x-l) = \theta_{n-1}$, and substituting into the expression for the discrete Laplacian $\partial_d^2\theta$, we get

$$\partial_d^2\theta = \partial_x^2\theta + \frac{l^2}{12}\partial_x^4\theta + O(\partial_x^6\theta). \tag{6}$$

The expression (6) is asymptotically correct only when the wave number $k \ll 1/l$, as can be readily seen from its Fourier transformation $[2\cos(kl) - 2]/l^2 = -k^2 + l^2k^4/12 + O(k^6)$, and breaks down when $kl \gg 1$, since $[2\cos(kl) - 2] \in [-4, 0]$, while $[-(kl)^2 + (kl)^4/12] \to +\infty$ as $k \to \infty$.

Substituting eqs. (1) and (6) into the expression (5) gives us

$$U(\theta) = \int_0^{\mathcal{L}} \left[-\frac{k_c l}{2}\theta\left(\partial_x^2\theta + \frac{l^2}{12}\partial_x^4\theta\right) + \frac{k_b}{2l}\theta^2\right]\mathrm{d}x. \tag{7}$$

To relate the plate deflection angle field $\theta$ to the concentration field of the binary fluid $\phi$, we note that in the uniform state, the reference concentration is $\phi_0 = (h-D)/l$. After the lamellae are deflected by $\theta$, the current concentration field is given by $\phi(x) = [h - (D - lL\partial_x\theta)]/l(1 - L\partial_x\theta) = \phi_0 + (2hL/l)\partial_x\theta + O[(\partial_x\theta)^2]$. Integrating $\phi(x)$ once allows us to write $\theta(x) = (l/2hL)\int_0^x \bar{\phi}\mathrm{d}x'$, where $\bar{\phi} = \phi - \phi_0$ is the difference between the current and the reference concentration. Substituting this into (7) gives us

$$U(\bar{\phi}) = \int_0^{\mathcal{L}} \left[-\frac{a_c}{2}\int_0^x \bar{\phi}\mathrm{d}x'\left(\partial_x\bar{\phi} + \frac{l^2}{12}\partial_x^3\bar{\phi}\right) + \frac{a_b}{2}\left(\int_0^x \bar{\phi}\mathrm{d}x'\right)^2\right]\mathrm{d}x, \tag{8}$$

where $a_c = k_c l^3/4h^2L^2$ and $a_b = k_b l/4h^2L^2$ are determined by capillarity and elasticity.

Substituting (8) into (4), we get the evolution equation,

$$\partial_t \bar{\phi} = a_0 a_c \partial_x^2 \left( \bar{\phi} + \frac{l^2}{12} \partial_x^2 \bar{\phi} \right) - a_0 a_b \bar{\phi}, \tag{9}$$

where the last term comes from the variation of the elastic bending energy[1]. To understand the onset of instability of the homogeneous vertical state, we derive the associated dispersion relation by substituting $\bar{\phi} = \exp(\omega t + ikx)$ into (9) to get

$$\omega = a_0 a_c \left( -k^2 + \frac{l^2}{12} k^4 \right) - a_0 a_b. \tag{10}$$

When $a_c < 0$, the fastest growing mode corresponds to the wave number $k_m = \sqrt{6}/l$ and the wavelength $\lambda_m \approx 2.57l$. We see that the continuum model qualitatively captures the primary mode of instability, although there is a quantitative discrepancy compared to the discrete model ($\lambda_m = 2l$), because the condition $kl \ll 1$ is not strictly satisfied. When $a_c > 0$, from (10) we see that $\omega \to \infty$ as $k \to \infty$ for any finite $a_b$. This failure to predict a stable state is inconsistent with both the experimental observations and the discrete model, because (6) breaks down when $kl \gg 1$. To fix this, we keep the first-order term in the expansion (6) when $a_c \geq 0$, so that $\omega = -a_0(a_c k^2 + a_b) < 0$. Therefore, (9) becomes

$$\partial_t \bar{\phi} = a_0 a_c \partial_x^2 \left( \bar{\phi} + a_1 l^2 \partial_x^2 \bar{\phi} \right) - a_0 a_b \bar{\phi}, \tag{11}$$

with $a_1$ modified to a piecewise constant, *i.e.* $a_1 = 1/2\pi^2$ when $a_c < 0$, and $a_1 = 0$ when $a_c \geq 0$ to capture the wavelength at the onset of instability.

Beyond the linear regime, we modify the functional form of the free energy $U(\bar{\phi})$ by adding a semi-phenomenological term into (8). Since the system can eventually separate into two phases of tips or gaps in the absence of an elastic field, the energy density should have two minima at $\phi = \pm 1$, suggesting a double-well potential $a_c(\phi^2/2 - \phi^4/4)$, as in the Cahn-Hilliard equation [11]. Indeed, a comparison with (8) suggests that $\phi^2$ may be a better alternative to $-(\int_0^x \bar{\phi} \mathrm{d}x')\partial_x \bar{\phi}$ (the first term in the right-hand side of (8)) as they have the same spectrum and the former has a smaller continuity requirement. The $\phi^4$ term is the first nonlinear term allowed by the symmetry of the system associated with $(\partial_x \theta)^4$ that was neglected in (7) and causes the pattern amplitude to saturate.

To account for the inhomogeneity of the liquid volume in the cells, we note that the capillary stiffness $k_c$ should be replaced by $k_c' = \sigma L f(\widetilde{V})$ with $f(\widetilde{V}) = c_c \widetilde{V}(\widetilde{V} - \widetilde{V}_c)$ being a dimensionless function that accounts for the nonmonotonic nature of the capillary force as a function of the dimensionless liquid volume $\widetilde{V} = V/DL$. Omitting the tilde henceforth for simplicity of notation, we note that

[1]This term looks nonconservative, but it is derived from $a_0 a_b \partial_x^2 [\int_0^x \mathrm{d}x_1 \int_0^{x_1} \bar{\phi}(x_2) \mathrm{d}x_2]$, which is in fact conservative.

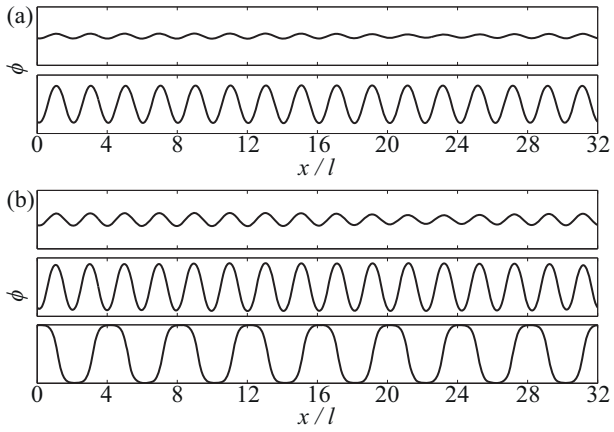


Fig. 2: The onset, evolution, and steady state of elastocapillary phase separation for an imposed homogenous liquid volume $V$, obtained by solving (12) on a periodic domain of length 32, corresponding to an array of 32 lamellae. A random perturbation with the amplitude of $\phi = 10^{-5}$ is prescribed as the initial condition. Using the parameters for the experiments shown in fig. 1, we set $c_c = 4500$, $V_c = 0.95$, $c_b = 10$, and $\phi_0 = 0$ in (12). All figures have the same scale, and the range of the vertical axis is $[-1, 1]$. (a) $V = 0.949$. The dimensionless wavelength of the primary mode is 2, and we see that the pattern saturates at a finite amplitude and stabilizes without coarsening. (b) $V = 0.8$. The pattern saturates at a finite amplitude by coarsening and stabilizing to form periodic domains of size 4.

when $V \geq V_c$, we get stable lamellae; when $V \leq V_c$, we get unstable lamellae; when $V \to 0$, $f(V) \to 0$, and we get stable lamellae again. Here the positive constant $c_c$ can be numerically computed from the discrete model to set the correct amplitude of $k_c'$, and $V_c = V_c(D/L)$ is the critical volume at which $k_c$ switches sign and can also be explicitly calculated.

Then the dimensionless form of (4) is given by

$$\begin{aligned} \partial_\tau \phi = \; & \partial_s^2 \Big[ c_c V (V - V_c) \left( \phi - \phi^3 + c_1 \partial_s^2 \phi \right) \Big] \\ & - c_b (\phi - \phi_0), \end{aligned} \tag{12}$$

where $\tau = t/t_c$, $t_c = 4h^2 L/a_0 \sigma l$ is the time scale at which lamellae deflect (coarsening time scale), $\partial_s = \partial/\partial s$, $s = x/l$, $c_b = k_b/\sigma L$, $c_1 = 0$ when $V \geq V_c$ and $c_1 = 1/2\pi^2$ when $V < V_c$. $V$ can be either a constant or a spatial and temporal function.

In fig. 2, we show the numerical solutions of eq. (12) using a spatially uniform $V$ as the control parameter with periodic boundary conditions and random perturbations of $V$ and/or $\phi$ as initial conditions, computed using the commercial finite element package COMSOL4.3a. We see that for $V < V_c$, phase separation results with either a finite amplitude and dimensionless wavelength 2 (fig. 2(a)) for small $f(V)$, or a hierarchically coarsened pattern with dimensionless wavelength 4 (fig. 2(b)) for large $f(V)$. Since $f(V)/c_b$ represents the ratio of capillary driving forces to the elastic bending resistance, the results show

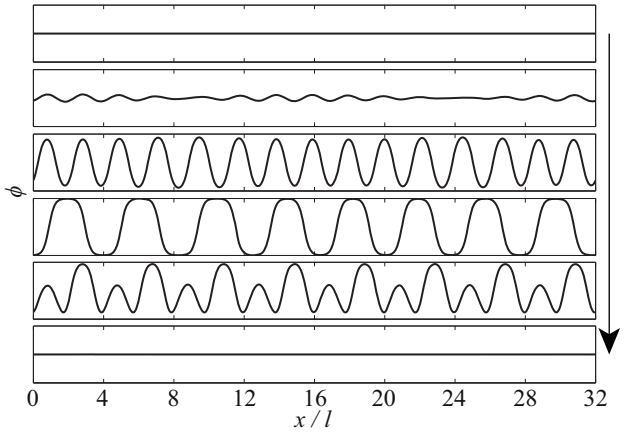


Fig. 3: The onset, evolution and steady state of elastocapillary phase separation coupled to evaporation dynamics obtained by solving (12) and (13) simultaneously. The initial conditions are $V = 1$ and $\phi = 0$, and an initial random perturbation of amplitude $\phi = 10^{-5}$ . Using the experimental parameters in fig. 1, we set $c_c = 4500$, $V_c = 0.95$, $c_b = 10$, $\phi_0 = 0$, $t_1 = 0.02\,\mathrm{s}$ and $t_2 = 0.2\,\mathrm{s}$. All figures have the same scale, and the range of the vertical axis is $[-1, 1]$. Time increases in the direction of the arrow, corresponding to dimensionless times $\tau$ are 0.64, 0.714, 0.8, 6, 58, and 140. At $\tau = 0.65$, $V > V_c$, and the system is still stable at $\phi = 0$. As $V$ decreases with time, the system becomes unstable to the primary mode of instability that gradually coarsens. An elastic refining process at very small $V$ appears naturally, as in the experimental observations, and corresponds to bundle separation. At late times, as $V \to 0$, *i.e.* when the liquid has almost completely evaporated, the system is restored to its initial state with $\phi = 0$.

that the largest bundle size depends on the competition between these two effects; indeed, for softer lamellae with smaller $k_b$, coarsening may continue beyond wavelength 4 until the increasing elastic resistance eventually arrests it.

If the dynamics of coalescence is coupled to evaporation, we need a dynamical law for the change in $V$. We assume that the evaporation rate is proportional to the area of the liquid-air interface and thus to both the local gap concentration $(1 - \phi)/2$ and the liquid volume $V$. Then, the dimensionless equation that governs the evolution of the liquid volume is

$$\partial_\tau V = \begin{cases} -\dfrac{t_c}{t_e}(1-\phi)V, & \text{when} \quad V > 0, \\ 0, & \text{otherwise}, \end{cases} \tag{13}$$

where $t_e$ is the evaporation time scale.

In fig. 3, we show the results for the case of the dynamics of lamella aggregation driven by an inhomogeneously evaporating liquid, obtained by solving (12) and (13) simultaneously with the same boundary and initial conditions used in fig. 2. The evaporation time scale and the coarsening time scale are well separated ($t_e = 10t_c$) so that $V$ decreases quasistatically. During the early stages of evaporation when $V > V_c$, the homogeneous state is insensitive to perturbations. When $V < V_c$, the dimensionless wavelength 2 in the unstable mode captures the dimerization observed in the experiments and the largest domain size 4 beyond the linear regime is also in good agreement with the observation of quadrimers (see fig. 1). Our model also naturally captures refining of domains when $V \approx 0$, describing the separation of bundles in the absence of interpillar adhesion. Then, the system is restored to its homogenous state $\phi = \phi_0$ on complete drying.

Our continuum model of dynamical coalescence driven by capillarity and eventually arrested by elasticity arises from a physically consistent discrete microscopic model. It captures the onset of instability and the primary unstable mode, and describes the dynamics of lamellar coalescence with elastic arrest, followed by the bundle separation, in terms of an elastocapillary field theory coupled to evaporation dynamics that accounts for long-wavelength inhomgeneities in space and time. Of particular significance is that all the coefficients in our model are directly linked to microscopically measurable physical and geometrical parameters in the experiments, allowing for a clear test of our theory.

More broadly, our continuum theory, eq. (12), is similar to the classical Cahn-Hilliard theory for phase separation [11] with an important difference due to the elastic contribution $\phi - \phi_0$. This term is the origin of the refining driven by elastic resistance that competes with the coarsening driven by surface tension. Together, they determine the stability of the system and arrest the coarsening at an equilibrium size. Given that aggregation dynamics with arrested phase separation is observed in a variety of physical systems, such as two-phase epitaxial monolayer grown on an elastic substrate [12–15] or phase separation in an electrochemically active nanoporous sponge [16], this class of theories ought to be broadly applicable. Indeed, a phenomenological model used to describe the evolution of nanoporosity in dealloying [16] is almost the same as eq. (12), although the underlying physics is fundamentally different and the model is not derived microscopically.

Natural generalizations of our model include accounting for the role of surface adhesion between contacting lamellae, and an anisotropic 2-dimensional theory for the coalescence of bristles [5] to capture the orthotropic and other symmetries in these systems.

* * *

We thank H.-Y. Kim for providing pictures of the experiments, T. Schneider for many discussions, and the Harvard-NSF, MRSEC, Wyss Institute and Kavli Institute for partial support.

## Appendix

For completeness, we briefly review the discrete model that serves as the basis for our mesoscopic continuum model.

The lamellae are modeled as rigid plates of unit depth elastically hinged at the base (fig. 4(a)). The hinge elastic constant can be approximately derived from the bending

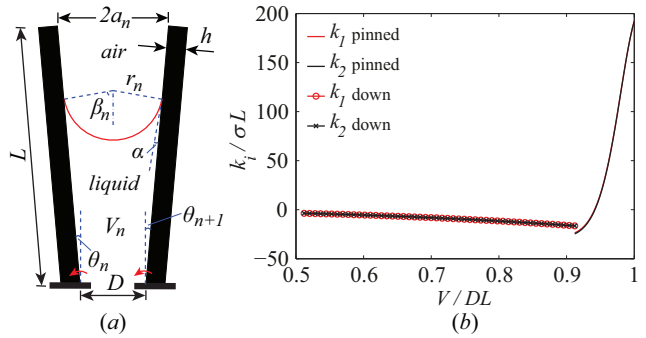


Fig. 4: (Colour on-line) (a) Sketch of the model of the $n$-th cell confined by two neighboring lamellae. The red curve represents the air-liquid interface. (b) Effective spring stiffness due to capillarity as a function of liquid volume for $L/D = 4$ at the homogeneous state where all pillars are vertical. When the meniscus is pinned at the plate tip, $k_2 = k_1 - \sigma L \sin\beta$. When the meniscus is down from the plate tip, $k_1 = k_2$. The discontinuity in $k_i$ corresponds to the meniscus sliding down from the tip.

response of a short cantilever by a transverse force $F$ at its free end, which is given by

$$k = \frac{\mathrm{d}(F\delta)}{\mathrm{d}\theta} = \frac{Eh^3}{3L}, \tag{A.1}$$

where $\delta = 4FL^3(1-\nu^2)/Eh^3$ is the deflection at the free end, and $\theta$ is the deflection angle of the plate with respect to the vertical direction.

The pressure field inside the liquid is considered as uniform. This assumption is based on two facts: 1) In our system, gravity can be neglected, because the Bond number $Bo \sim 10^{-5} \ll 1$ indicates that the gravity is dominated by surface tension. 2) Comparing the viscous torque acting on the plate due to flow $M_\mu \sim \mu L^5 \dot{\theta}/D^3$ with that caused by the surface tension $M_\sigma \sim \sigma L^2/D$, where $\mu$ is the viscosity of the fluid and $\dot{\theta}$ is the angular velocity of the rotating plate, we find that $M_\mu/M_\sigma \sim 10^{-3} \ll 1$ for $\dot{\theta} \sim O(1)$, which indicates that pressure effects due to fluid flow can be neglected. Therefore, the air-liquid interface can be well approximated by a circular arc because of the uniform pressure in each cell.

We assume the contact angle to be arbitrary when the meniscus is pinned on the tip, as long as it is larger than the critical value $\alpha$. The meniscus can thus be concave-up, flat, or concave-down. Once the contact angle reaches $\alpha$, it remains constant at $\alpha$ as the meniscus slides down from the tip.

Consequently, the meniscus profile and the resulting moment $M_n$ can be calculated for any given deflection angles $\theta_n$, $\theta_{n+1}$ (counterclockwise is positive) and the liquid volume per unit depth $V_n$. We include the following results that are necessary for our subsequent derivation of capillary stiffnesses.

For the case when the meniscus is pinned on both tips, The moments on the $n$-th and $(n+1)$-th plates are given, respectively, by

$$M_n = -\frac{1}{2a_n}\big[\sin(\beta_n + \theta_n - \theta_{n+1}) + d\cos(\beta_n + \theta_n)\big], \tag{A.2}$$

$$M_{n+1} = \frac{1}{2a_n}\big[\sin(\beta_n + \theta_n - \theta_{n+1}) + d\cos(\theta_{n+1} - \beta_n)\big], \tag{A.3}$$

where $2\beta_n$ is the angle subtended by the meniscus arc, $d = D/L$, and $2a_n$ is the tip separation. $\beta_n$ is determined by solving

$$\frac{V_n}{L^2} = \frac{1}{2}d(\cos\theta_n + \cos\theta_{n+1}) + \frac{1}{2}\sin(\theta_n - \theta_{n+1}) - a_n^2(\beta_n \csc^2\beta_n - \cot\beta_n), \tag{A.4}$$

for given $V_n$, $\theta_n$ and $\theta_{n+1}$, and

$$2a_n = \big[2 - 2\cos(\theta_{n+1} - \theta_n) + d^2 + 2d(\sin\theta_n - \sin\theta_{n+1})\big]^{\frac{1}{2}}. \tag{A.5}$$

$\beta_n$ must satisfy $\beta_n \le \beta_n^*$, where $\beta_n^*$ is the critical angle at which the meniscus starts to slide down from at least one lamella. $\beta_n < 0$ when the meniscus concaves down, $\beta_n = 0$ when the meniscus is flat, and $\beta_n > 0$ when the meniscus concaves up.

For the case when the meniscus is down from both tips, and $\theta_n = \theta_{n+1} = \theta$, the moments on the $n$-th and $(n+1)$-th plate are given, respectively, by

$$\begin{aligned} M_n &= -\frac{L_{wrn}^2}{2r_n} - L_{wrn}\sin\alpha, \\ M_{n+1} &= \frac{L_{wln+1}^2}{2r_n} + L_{wln+1}\sin\alpha, \end{aligned} \tag{A.6}$$

where the meniscus radius $r_n = d\cos\theta/(2\cos\alpha)$, and the wetting length on the right side of the $n$-th plate, $L_{wrn}$, and that on the left side of the $(n+1)$-th plate, $L_{wln+1}$, are given, respectively, by

$$\begin{aligned} L_{wrn} &= l_n - \frac{d}{2}\cos\theta\tan\alpha, \\ L_{wln+1} &= l_n - \frac{d}{2}\cos\theta\tan\alpha + d\sin\theta. \end{aligned} \tag{A.7}$$

$l_n$ is determined by solving

$$\frac{V_n}{L^2} = \frac{2l_n + d\sin\theta}{2}d\cos\theta - \left(\frac{d\cos\theta}{2}\right)^2\tan\alpha - \frac{\pi - 2\alpha}{2}\left(\frac{d\cos\theta}{2\cos\alpha}\right)^2. \tag{A.8}$$

So far, we have only calculated the moments based on a 2-plate model. To get the total moment on one plate, we must add the contributions from both adjacent cells. For example, we can obtain the full expression of $M_n$ simply

by replacing $n$ by $n-1$ in eq. (A.3) and add up to eq. (A.2) for the case in which the meniscus is pinned at both tips, which readily yields $M_n = M_n(\theta_{n-1}, \theta_n, \theta_{n+1}, V_n, V_{n-1})$.

For a periodic domain of $2N$ vertical lamellae and the same volume of liquid $V$ confined in each cell, the stiffness matrix of the system $\mathrm{d}\overrightarrow{M}/\mathrm{d}\overrightarrow{\theta}$ is given by

$$\begin{bmatrix} \ddots & \vdots & \vdots & \vdots & \vdots & \vdots & \\ \dots & -k_1 & 2k_2 & -k_1 & 0 & 0 & \dots \\ \dots & 0 & -k_1 & 2k_2 & -k_1 & 0 & \dots \\ \dots & 0 & 0 & -k_1 & 2k_2 & -k_1 & \dots \\ & \vdots & \vdots & \vdots & \vdots & \vdots & \ddots \end{bmatrix}, \tag{A.9}$$

where $\overrightarrow{M}$ is the vector of moments on all plates and $\overrightarrow{\theta}$ is the vector of deflection angles of all plates, and $k_1(\sigma L, V/L^2)$ and $k_2(\sigma L, V/L^2)$ are the capillary stiffnesses. The eigenvalues $s(f)$ and eigenvectors $\Psi(f)$ of $\mathrm{d}\overrightarrow{M}/\mathrm{d}\overrightarrow{\theta}$ thus are given by

$$\begin{aligned} s(f) &= -2k_1\cos(f) + 2k_2 + k_b, \\ \Psi(f) &= \left[1, e^{if}, e^{2if}, \dots, e^{i(2N-3)f}, e^{i(2N-2)f}, e^{-if}\right], \end{aligned} \tag{A.10}$$

respectively, where $f = n\pi/N$ with $n = 1, 2, \dots, 2N$.

For the case in which the meniscus is pinned at both tips,

$$\begin{aligned} \frac{k_1}{\sigma L} &= \frac{\cos\beta - d\sin\beta}{d}\left[1 + \frac{1 - d(\beta\csc^2\beta - \cot\beta)}{d^2\csc^2\beta(1 - \beta\cot\beta)}\right] \\ &\quad - \frac{\sin\beta + d\cos\beta}{d^2} + \sin\beta, \\ k_2 &= k_1 - \sigma L\sin\beta, \end{aligned} \tag{A.11}$$

where $d = D/L$, and $2\beta$ is the angle subtending the meniscus arc and is determined by the volume

$$\frac{V}{L^2} = d - \left(\frac{d}{2}\right)^2(\beta\csc^2\beta - \cot\beta). \tag{A.12}$$

For the case in which the meniscus is no longer at both tips,

$$\begin{aligned} \frac{k_1}{\sigma L} &= -\left[\frac{L_c}{r}\sin\alpha + \frac{L_c^2}{2r^2} + \sin^2\alpha\right]\frac{2L_c + d\tan\alpha}{4\cos\alpha}, \\ k_1 &= k_2, \end{aligned} \tag{A.13}$$

where $r = d/(2\cos\alpha)$ is the radius of the meniscus, and the contact line position $L_c$ is determined by the volume

$$\frac{V}{L^2} = L_c d + d^2\tan\left(\frac{\alpha}{4}\right) - d^2\frac{\pi - 2\alpha}{8\cos^2\alpha}. \tag{A.14}$$

We take $k_1 = k_2 = k_c$ for simplicity henceforth, as in eq. (A.11) $\sigma L\sin\beta/k_1 \ll 1$ for the parameter space that we are interested in.

Only key expressions relevant to this paper are listed here, while the complete details are given in [10].

REFERENCES


[1] Grzybowski B., Stone H. A. and Whitesides G. M., *Nature*, **405** (2000) 1033.

[2] Grzybowski B. A., Jiang X., Stone H. A. and Whitesides G. M., *Phys. Rev. E*, **64** (2001) 11603.

[3] Tanaka T., Morigami M. and Atoda N., *Jpn. J. Appl. Phys.*, **32** (1993) 6059.

[4] Bico J., Roman B., Moulin L. and Boudaoud A., *Nature*, **432** (2004) 690.

[5] Pokroy B., Kang S. H., Mahadevan L. and Aizenberg J., *Science*, **323** (2009) 237.

[6] Chandra D., Yang S., Soshinsky A. A. and Gambogi R. J., *ACS Appl. Mater. Interfaces*, **1** (2009) 1698.

[7] Boudaoud A., Bico J. and Roman B., *Phys. Rev. E*, **76** (2007) 060102.

[8] Gat A. D. and Gharib M., *J. Fluid Mech.*, **723** (2013) 692.

[9] Ashcroft N. W. and Mermin N. D., *Solid State Physics* (Thomson Press (India) Ltd.) 2003.

[10] Wei Z., Schneider T., Kim J., Kim H. Y., Aizenberg J. and Mahadevan L., *Elastocapillary instability, dynamical collapse and arrest of microscopic lamellae and pillars*, unpublished.

[11] Cahn J. W. and Hilliard J. E., *J. Chem. Phys.*, **28** (1958) 258.

[12] Kern K., Niehus H., Schatz A., Zeppenfeld P., Goerge J. and Comsa G., *Phys. Rev. Lett.*, **67** (1991) 855.

[13] Pohl K., Bartelt M. C., de la Figuera J., Bartelt N. C., Hrbek J. and Hwang R. Q., *Nature*, **397** (1999) 238.

[14] Röder H., Schuster R., Brune H. and Kern K., *Phys. Rev. Lett.*, **71** (1993) 2086.

[15] Lu W. and Suo Z., *J. Mech. Phys. Solids*, **49** (2001) 1937.

[16] Erlebacher J., Aziz M., Karma A., Dimitrov N. and Sieradzki K., *Nature*, **410** (2001) 450.